nature photonics

Article

https://doi.org/10.1038/s41566-024-01461-8

A solution-processable natural crystal with giant optical anisotropy for efficient manipulation of light polarization

Received: 12 January 2024

Accepted: 9 May 2024

Published online: 14 June 2024

Check for updates

Yang Zhou[1,2], Zhengfeng Guo[3,4], Honggang Gu[3,4] ✉, Yanqiang Li[1,2], Yipeng Song[1,2], Shiyuan Liu[3,4], Maochun Hong[1], Sangen Zhao[1,2] ✉ & Junhua Luo[1,2] ✉

Optical anisotropy, a spatially asymmetric light–matter interaction that manifests itself as birefringence and dichroism, is paramount for manipulating light polarization in modern optics. So far, various natural birefringent crystals are widely used, but their birefringence is limited to <0.3. Here we demonstrate a solution-processable natural crystal $C_3H_8N_6I_6{\cdot}3H_2O$ with giant birefringence up to 2.8 within the visible to infrared spectral region. Combining critical point analysis and the first-principles calculations, we reveal that this giant optical anisotropy mainly comes from the linear $(I_3)^-$ structural units in a parallel arrangement, which maximizes the difference of polarizability along the different crystallographic axes. This work highlights the potential of natural polyiodide crystals as an outstanding platform to satisfy the increasing demand for photonic applications that exploit polarization in optical communication, three-dimensional imaging, ultrahigh-resolution sensing and other tasks.

Since the discovery of the birefringence phenomenon three centuries ago[1,2], optical anisotropy has been widely used in light manipulation, such as photonic devices, remote sensing and polarization imaging[3–5]. The propagation of light in a non-homogeneous material can be expressed by the complex refractive indices ($N = n + i\kappa$). The real part represents the refractive indices, and the imaginary part represents the absorption coefficients. Birefringence (Δn, difference in refractive indices) and dichroism ($\Delta\kappa$, difference in absorption coefficients) are important parameters for quantifying the optical anisotropy of materials. Over the past years, birefringence and/or dichroism have been discovered in numerous materials[6–11]. Despite its importance for high-performance optics, the anisotropy of commercial crystals remains relatively small, with the current maximum birefringence of commercial crystals approximating 0.3 (refs. 6–10). To fabricate compact and efficient polarizing optical devices, natural bulk crystals with large optical anisotropy have attracted increasing attention in recent years[10,12–14]. The record holder is $BaTiS_3$, with a birefringence of 0.76 in the mid-infrared spectral regions and a degree of linear polarization (DLP) of 0.9 in the visible spectral region[13]. Meanwhile, researchers found that the differences in intra-layer and inter-layer bonding are responsible for the highly anisotropic nature of atomically thin van der Waals layered materials[15,16], such as *h*-BN[17], α-MoO_3[18], α-V_2O_5[19], ReS_2[20], $GeSe_2$[21], Sb_2Se_3[22] and black phosphorus[23]. In particular, MoS_2 possesses a giant birefringence of 1.5 in the infrared spectral region and 3.0 in the visible light[24]. Nevertheless, their applications are hindered by the lack of large in-plane optical anisotropy (Supplementary Table 1). In addition, large optical anisotropy can be provided in metamaterials and metasurfaces by artificially engineered means[25,26], but optical losses and manufacturing challenges hinder their widespread use.

[1]State Key Laboratory of Structural Chemistry, Fujian Institute of Research on the Structure of Matter, Chinese Academy of Sciences, Fuzhou, China. [2]University of Chinese Academy of Sciences, Beijing, China. [3]State Key Laboratory of Intelligent Manufacturing Equipment and Technology, School of Mechanical Science and Engineering, Huazhong University of Science and Technology, Wuhan, China. [4]Optics Valley Laboratory, Hubei, China. ✉e-mail: hongganggu@hust.edu.cn; zhaosangen@fjirsm.ac.cn; jhluo@fjirsm.ac.cn

https://doi.org/10.1038/s41566-024-01461-8

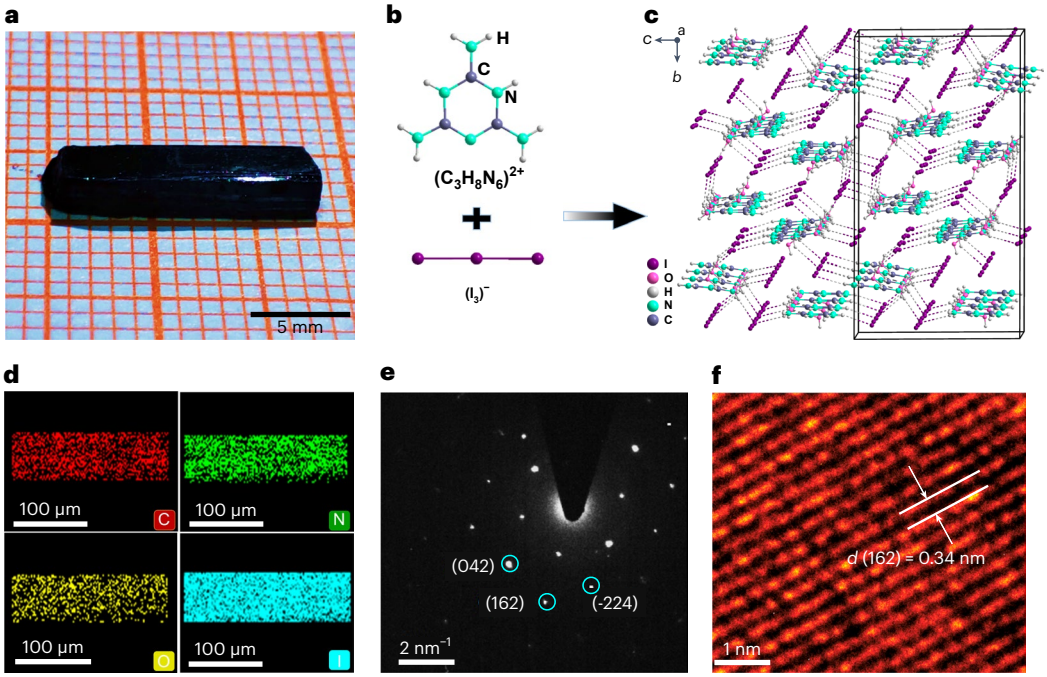

Fig. 1 | Structure and optical images of $C_3H_8N_6I_6{\cdot}3H_2O$ crystal. a, The as-grown bulk crystal of $C_3H_8N_6I_6{\cdot}3H_2O$ with sizes of 13 mm × 4 mm × 2 mm. Scale bar, 5 mm. **b**, $(C_3H_8N_6)^{2+}$ cationic ring and linear $(I_3)^-$ anion. **c**, $C_3H_8N_6I_6{\cdot}3H_2O$ crystal structure viewed along the *a* axis. The dashed lines represent hydrogen bonding. **d**, The elemental mapping of $C_3H_8N_6I_6{\cdot}3H_2O$. Scale bar, 100 μm. **e**, The selected-area electron diffraction pattern of $C_3H_8N_6I_6{\cdot}3H_2O$. ((042), (162) and (−224) represent different crystal face indices of $C_3H_8N_6I_6{\cdot}3H_2O$). Scale bar, 2 nm^{-1}. **f**, Enlarged HRTEM image. Scale bar, 1 nm.

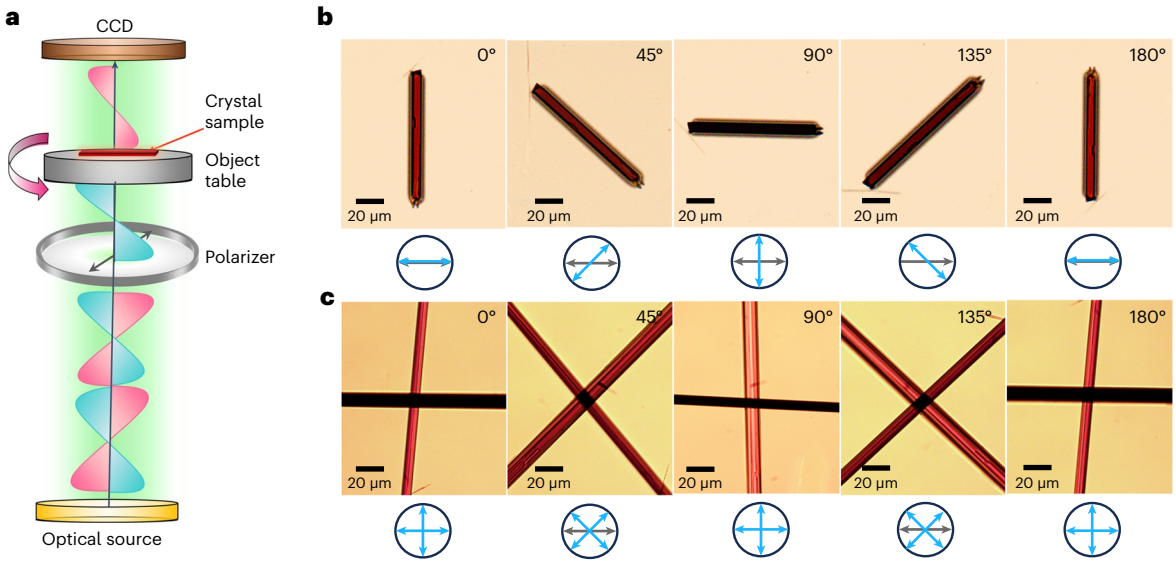

Fig. 2 | Visualized optical anisotropy of $C_3H_8N_6I_6{\cdot}3H_2O$. a, Schematic diagram of polarizing microscope. **b**, Single-crystal images of $C_3H_8N_6I_6{\cdot}3H_2O$ crystal at different polarization angles from 0° to 180°. **c**, Images of two vertically crossed $C_3H_8N_6I_6{\cdot}3H_2O$ single crystals at different polarization angles from 0° to 180°. Grey arrows represent the orientation of polarized light; blue arrows represent the orientation of the polarization of single crystals.

In this article, we report a new natural bulk crystal $C_3H_8N_6I_6{\cdot}3H_2O$, which exhibits giant anisotropic optical properties with birefringence up to 2.8 in the visible spectral region, 1.7 in the near-infrared spectral region, and ultrahigh linear dichroism with the DLP reaches 0.98. A systematic method based on critical point (CP) analysis and first-principles calculations is proposed to reveal the structure and excellent optical performance of $C_3H_8N_6I_6{\cdot}3H_2O$.

Centimetre-sized $C_3H_8N_6I_6{\cdot}3H_2O$ single crystals were grown by the solution cooling method. To characterize the chemical composition, chemical structure and quality of the crystals, we used single-crystal X-ray diffraction (XRD), powder XRD, energy-dispersive X-ray spectroscopy (EDS) and high-resolution transmission electron microscopy (HRTEM) to characterize the synthesized $C_3H_8N_6I_6{\cdot}3H_2O$ crystals. The as-grown bulk crystal is shown in Fig. 1a. Its phase purity was proved by powder XRD (Supplementary Fig. 1). According to the single-crystal XRD data, $C_3H_8N_6I_6{\cdot}3H_2O$ crystallizes in the monoclinic space group $P2_1/n$ (No. 14) with lattice parameters of $a = 9.487\ (2)$ Å, $b = 27.266\ (3)$ Å, $c = 14.989\ (2)$ Å, $\beta = 97.9031°$ and $V = 3840.71$ Å^3 (for crystallographic details, see Supplementary Tables 2–5). $C_3H_8N_6I_6{\cdot}3H_2O$ crystal structure mainly consists of melamine organic cation $(C_3H_8N_6)^{2+}$ and inorganic

https://doi.org/10.1038/s41566-024-01461-8

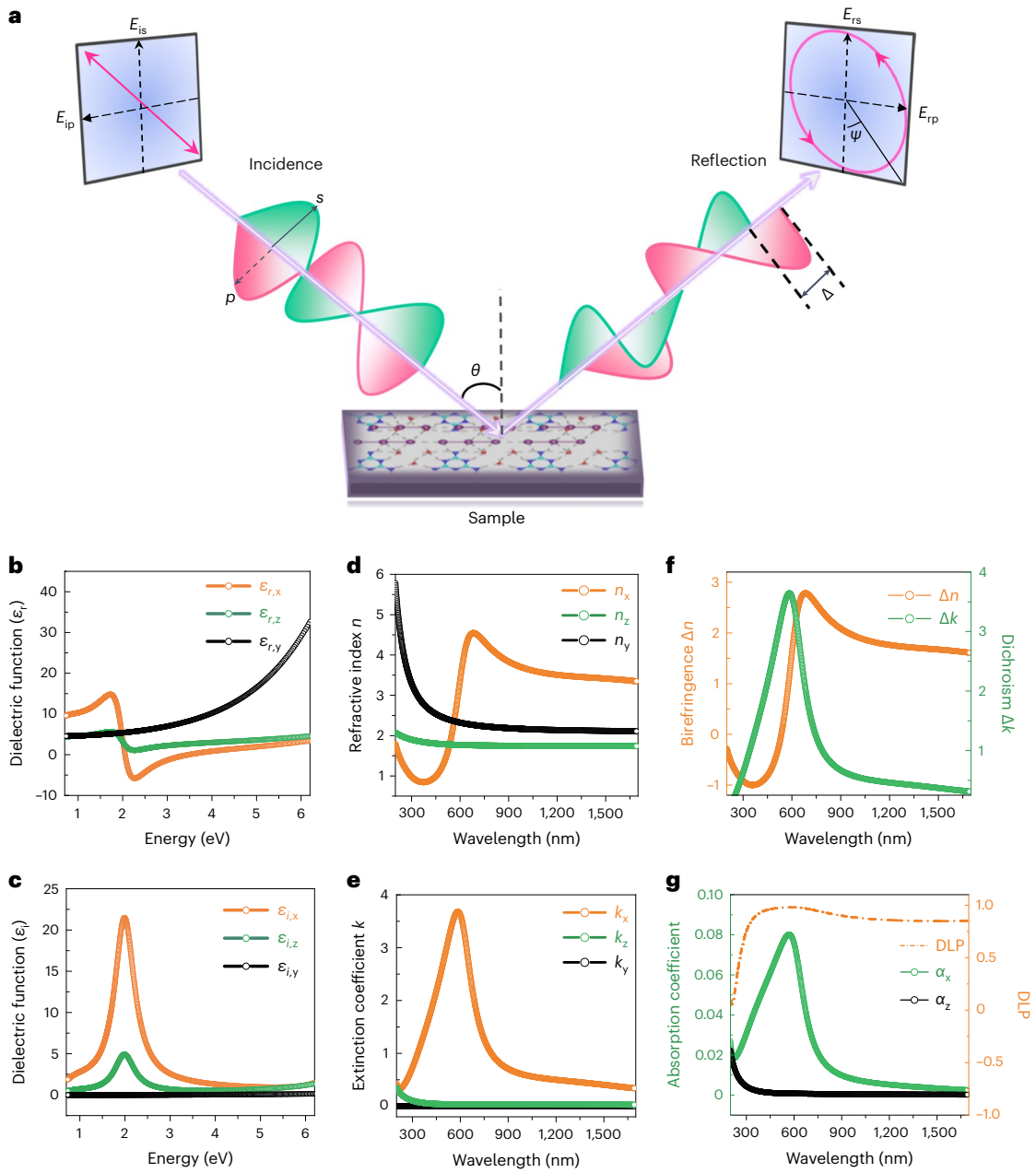

Fig. 3 | Dielectric and optical anisotropy of $C_3H_8N_6I_6{\cdot}3H_2O$. a, The working principle of Mueller matrix spectroscopic ellipsometer. θ represents the incident angle. The Mueller matrix is obtained by rotating compensators: *p* and *s* polarization states, which refer to the linearly polarized light parallel and perpendicular to the incident plane, respectively. **b**, The real part of the dielectric tensor of $C_3H_8N_6I_6{\cdot}3H_2O$. **c**, The imaginary part of the dielectric tensor of $C_3H_8N_6I_6{\cdot}3H_2O$. **d**,**e**, The experimental refractive indices (**d**) and extinction coefficients (**e**) of $C_3H_8N_6I_6{\cdot}3H_2O$ along *x*, *y* and *z* axes. **f**, Experimental birefringence and dichroism of $C_3H_8N_6I_6{\cdot}3H_2O$. **g**, Absorption coefficients in response to the *x* and *z* axis, and the DLP over the entire measured range.

linear $(I_3)^-$ anion (Fig. 1b). The $(I_3)^-$ anions are stacked end-to-end along the *a* axis, forming an infinite linear chain with a distance of $(I_3)^-\cdots(I_3)^-$ of about 3.65 Å, which is much larger than the distance of I–I in the linear $(I_3)^-$ chain (2.8583(8) Å to 3.0764(8) Å). In comparison, the bonding distance of the I–I distance is ≤3.2 Å (Supplementary Fig. 2a)[27]. In addition, adjacent $(C_3H_8N_6)^{2+}$ cations are connected by forming hydrogen bonds with water molecules (H-O···H ≤2.53 Å) and evenly interspersed in polyiodide infinite chains (Fig. 1c and Supplementary Fig. 2b). Considering a more stable crystal stacking, the hydrogen bonds (N–H···I ≤2.95 Å) between $(C_3H_8N_6)^{2+}$ and $(I_3)^-$ acts as a linkage. The EDS spectra (Supplementary Fig. 3) show no irrelevant signals except those from the transmission electron microscopy Cu grid, demonstrating the high purity of $C_3H_8N_6I_6{\cdot}3H_2O$ crystal. Figure 1d illustrates the EDS mapping, demonstrating a uniform distribution of C, N, I and O elements. The selected area electron diffraction pattern (Fig. 1e) indicates that $C_3H_8N_6I_6{\cdot}3H_2O$ crystal has high crystallinity. The crystal planes correlating with the brightest spots are labelled, that is, (042), (162) and (−224). In addition, the lattice fringing observed in the magnified HRTEM image from Fig. 1f further confirms its single-crystal nature of $C_3H_8N_6I_6{\cdot}3H_2O$, and the interplanar distance is 0.34 nm, consistent with the (162) lattice plane. A single crystal of $C_3H_8N_6I_6{\cdot}3H_2O$ with a thickness of about 2 mm was measured for surface laser-induced damage threshold (LIDT). Supplementary Fig. 4 shows $C_3H_8N_6I_6{\cdot}3H_2O$ single-crystal surface before and after laser damage under an optical microscope. The LIDT of $C_3H_8N_6I_6{\cdot}3H_2O$ single crystal is 114.9 MW cm^{-2} using an incident laser at 1064 nm, 10 ns and 1 Hz, which is about

https://doi.org/10.1038/s41566-024-01461-8

13 times that of commercial $AgGaS_2$ crystal (9.0 MW cm^{-2})[28] at the same measurement conditions. Moreover, we have also characterized the hardness of $C_3H_8N_6I_6{\cdot}3H_2O$ single crystal. As shown in Supplementary Fig. 5, a diamond square cone indenter pressed into the crystal surface produces a well-defined indentation pit, corresponding to a Vickers hardness of 12.2, which indicates that the $C_3H_8N_6I_6{\cdot}3H_2O$ crystal is easy to cut.

To understand the anisotropic nature of $C_3H_8N_6I_6{\cdot}3H_2O$ crystals, we first characterized $C_3H_8N_6I_6{\cdot}3H_2O$ crystals under a polarizing microscope, where the upper polarizer is kept closed throughout the testing period. Figure 2a shows a schematic diagram of the test setup for a polarizing microscope. The $C_3H_8N_6I_6{\cdot}3H_2O$ single crystal exhibits noticeable periodic bright and dark changes with the changes of polarization angles (Fig. 2b). Specifically, the $C_3H_8N_6I_6{\cdot}3H_2O$ crystal is brightest at polarization angles of 0° and 180° (parallel to the direction of polarized light) and darkest at a polarization angle of 90° (perpendicular to the direction of polarized light). For any crystal orientation, the brightness is uniform across the crystal, indicating that the crystal comprises a single orientational domain. Furthermore, when we cross two crystals vertically (Fig. 2c), the non-overlapping domains of the two crystals show periodic changes in brightness and darkness as the polarization angle changes. However, the overlapping domain remains dark regardless of the polarization angle. Supplementary Videos 1 and 2 provide recorded images of $C_3H_8N_6I_6{\cdot}3H_2O$ crystals. The observed dependence of $C_3H_8N_6I_6{\cdot}3H_2O$ single crystal on the change of bright and dark is directly analogous to a polarizer. This phenomenon indicates that $C_3H_8N_6I_6{\cdot}3H_2O$ crystal exhibits important optical anisotropy.

In an attempt to comprehensively quantify the magnitude of the optical anisotropy, we obtained the complete dielectric tensor of bulk $C_3H_8N_6I_6{\cdot}3H_2O$ crystal by matching measured ellipsometric spectra with a well-established optical model[29] using a Mueller matrix spectroscopic ellipsometer[30]. $C_3H_8N_6I_6{\cdot}3H_2O$ crystal faces are determined by an Agilent Bruker D8 diffractometer to confirm the direction of the crystal axis further (Supplementary Fig. 6). The working principle of the Mueller matrix spectroscopic ellipsometer is shown in Fig. 3a and Supplementary Fig. 7. More details can be found in Supplementary Information. We employed the 4 × 4 matrix method to simulate Mueller matrix spectra and found excellent agreement between the simulated curves and experimental data (Supplementary Fig. 8).

The optical properties of $C_3H_8N_6I_6{\cdot}3H_2O$ are extracted from the Mueller matrix measured in the wavelength range from 200 nm to 1,690 nm (Fig. 3b,c). Over the entire measurement range, the diagonal dielectric tensor represents the real (ε_r) and imaginary (ε_i) parts of the dielectric constant. Meanwhile, we extracted wavelength-dependent refractive indices, extinction coefficients, birefringence and linear dichroism (Fig. 3d–g). These results are consistent with the first-principles calculations as shown in Supplementary Figs. 9 and 10. Clearly, Fig. 3f displays giant birefringence of $C_3H_8N_6I_6{\cdot}3H_2O$ with $\Delta n \approx 2.8$ in the visible region and $\Delta n \approx 1.7$ in the near-infrared region. To our knowledge, the birefringence of $C_3H_8N_6I_6{\cdot}3H_2O$ is comparable to that of the most birefringent 2D material MoS_2[24] and several times larger than $BaTiS_3$[13] and even reaches about one order of magnitude larger than those of commercial and other birefringent crystals[13,31–35], such as calcite[6], quartz[6], TiO_2[7] and α-BaB_2O_4[9] (Fig. 4).

Importantly, $C_3H_8N_6I_6{\cdot}3H_2O$ displays an ultrahigh linear dichroism $\Delta k \approx 3.7$ in the measured wavelength range, which is significantly larger than those of strongly optical anisotropic materials, such as $BaTiS_3$ ($|\Delta k| < 1.5$ from the visible to infrared spectral region)[13], MoS_2 ($\Delta k < 3.0$ from the visible to infrared spectral region)[24] and Ta_2NiS_5 ($\Delta k < 2.0$ from the visible to infrared spectral region)[36]. The linear dichroism of $C_3H_8N_6I_6{\cdot}3H_2O$ is further evaluated by introducing the DLP. Here, DLP is defined as $(\alpha_x - \alpha_z)/(\alpha_x + \alpha_z)$, which has values within the range from −1 to 1. We extracted the absorption coefficients along x and z axes in the 200–1,690 nm range based on the complex refractive index. The absorption coefficient along the x axis of $C_3H_8N_6I_6{\cdot}3H_2O$ crystals is much stronger than that along the z axis over a wide range of wavelengths (Fig. 3g). It exhibits ultrahigh linear dichroism with a DLP close to 0.98. This DLP is much higher than those of other natural materials with strong linear dichroism, including black phosphorus (DLP ~0.2)[37], $PdSe_2$ (DLP ~0.09)[38] and $BaTiS_3$ (DLP ~0.9)[13,39].

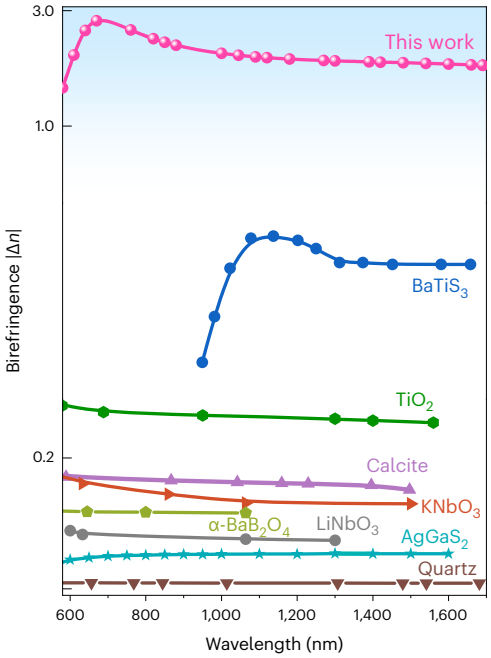

Fig. 4 | Comparison of birefringence. Comparison of the birefringence of $C_3H_8N_6I_6{\cdot}3H_2O$ with different birefringent materials, including $BaTiS_3$[13], TiO_2[7], calcite[6], quartz[6], α-BaB_2O_4[9], $LiNbO_3$[33], $KNbO_3$[34] and $AgGaS_2$[35].

To demystify the underlying relationship between the structure and optical performance of $C_3H_8N_6I_6{\cdot}3H_2O$, we performed CP analyses on the dielectric functions by diagonal matrix elements. Since the imaginary part of the dielectric function, ε_y, is zero at the measured wavelength range, there is no optical absorption and electron transition in y axes. Here, we only consider the optical transition in ε_x and ε_z. Figure 5a and Fig. 5c show the second derivative of dielectric functions $d^2\varepsilon/dE^2$ and the best-fitting curves along the ε_x and ε_z, respectively. Supplementary Tables 6 and 7 list the corresponding parameters of the best-fit curves, including the specific type, shape and centre energy position of the CP[40,41]. The second derivative of dielectric function spectra along x and z axes show almost the same curve trend. However, their peaks are significantly different, which further explains the giant optical anisotropy along x and z axes.

The energy differences (E_{C-V}) from the valence band to the conduction band serve as a bridge connecting CPs to band structure and partial density of states (DOS) and are the key to revealing the origin of CPs[42,43]. As demonstrated in Supplementary Fig. 11a, the bandgap of $C_3H_8N_6I_6{\cdot}3H_2O$ is 1.84 eV, which is consistent with the experimental value (Supplementary Fig. 11b). Here, we consider that the electrons are difficult to excite, so only the highest-valence bands (V1–V5) are under consideration. In Fig. 5 and Supplementary Fig. 12, the CP A_x and A_z at centre energy (E_0) of 2.0 eV involve transitioning from V5 to C5 between A and B points in the Brillouin zone. Both the CPs along x and z axes are attributed to the jump of electrons in the 5p orbitals of I atoms from the top of the valence bands to the bottom of the conduction bands (Fig. 5b,d). In other words, the giant optical anisotropy of $C_3H_8N_6I_6{\cdot}3H_2O$ mainly comes from the 5p orbital of I atoms from the perspective of quantum mechanics. Moreover, based on the first-principles studies, we calculated the polarizability anisotropy for different building units in different birefringent crystals (Supplementary Fig. 13). It is clear that linear $(I_3)^-$ has a much larger polarizability anisotropy than other

https://doi.org/10.1038/s41566-024-01461-8

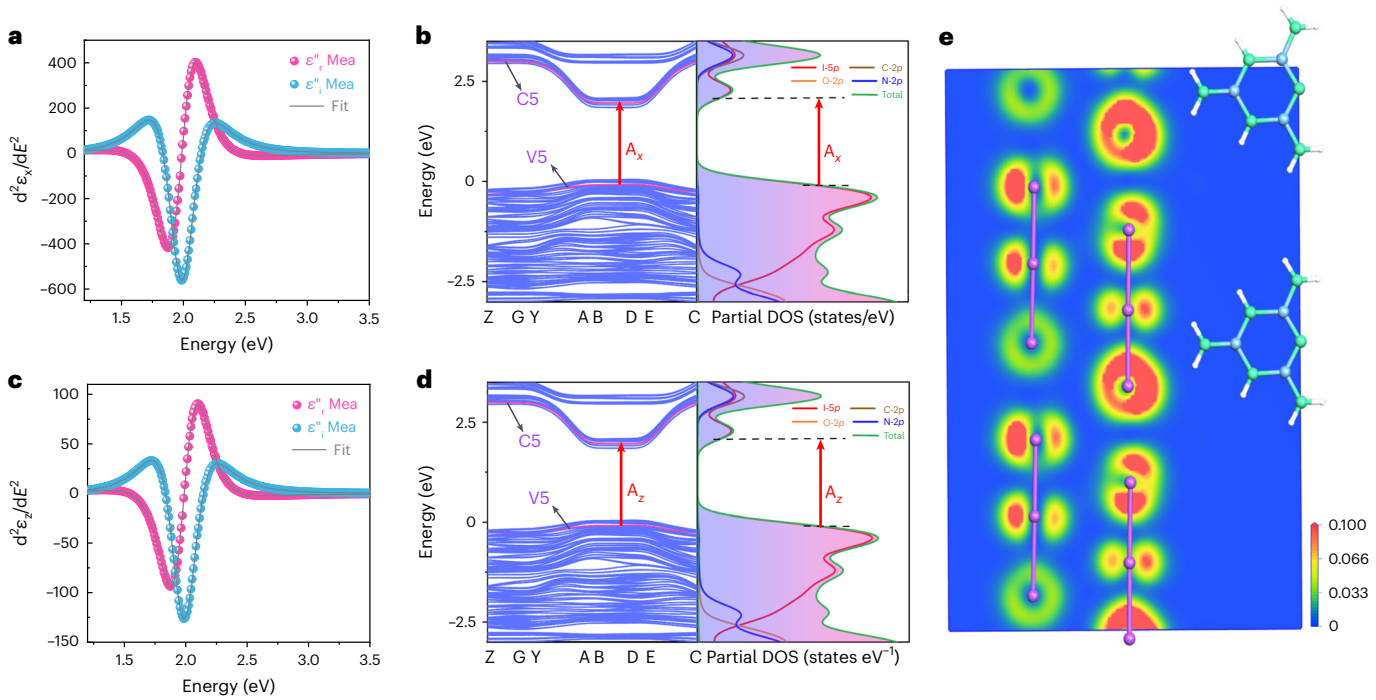

Fig. 5 | Theoretical analysis of $C_3H_8N_6I_6{\cdot}3H_2O$. a,**c**, The second derivative of fitted dielectric functions along ε_x (**a**) and ε_z (**c**) of $C_3H_8N_6I_6{\cdot}3H_2O$. (Here, the Mea. is defined as measured.) **b**,**d**, The interband transitions in the band structure (left) and partial DOS (right) along ε_x (**b**) and ε_z (**d**) of $C_3H_8N_6I_6{\cdot}3H_2O$. C5, conduction band. V5, valence band. For A_x and A_z, the CP at E_0 of 2.0 eV involves transitioning from V5 to C5 and between A and B points in the Brillouin zone along *x* and *z* axes, respectively. **e**, The projection of the ELF on (010) crystal plane for $C_3H_8N_6I_6{\cdot}3H_2O$. The iso-value increases from blue to red, and the maximum ELF value is scaled to 0.1.

π-conjugated building units including the $(C_3H_8N_6)^{2+}$ ring, indicating that linear $(I_3)^-$ makes much more contributions to the birefringence.

In addition, we further reveal the mechanism of giant optical anisotropy from the microscopic point of view. We performed the electron localization function map projected on (010) crystal plane[44], the highest occupied molecular orbitals (HOMO) and lowest unoccupied molecular orbitals (LUMO) in the structure of $C_3H_8N_6I_6{\cdot}3H_2O$. The electron cloud density in $C_3H_8N_6I_6{\cdot}3H_2O$ is primarily concentrated on the $(I_3)^-$ anion chain and exhibits an ellipsoidal shape, resulting in strong optical anisotropy as shown in the electron localization function map (Fig. 5e). Moreover, Supplementary Fig. 14 shows that there are two different $(I_3)^-$ anion chains occupying the HOMO and LUMO, respectively, which intuitively demonstrates that $(I_3)^-$ anions are mainly responsible for the giant optical anisotropy. The perfect parallel arrangement of linear $(I_3)^-$ further maximizes the optical anisotropy of $C_3H_8N_6I_6{\cdot}3H_2O$ from the perspective of the structure–property relationship.

In conclusion, we have discovered and grown a new natural bulk crystal, $C_3H_8N_6I_6{\cdot}3H_2O$, which possesses giant birefringence up to 2.8 from the visible to infrared spectral region, about 3.7 times larger than that of record-holder $BaTiS_3$. Moreover, its linear dichroism shows an ultrahigh DLP 0.98. As a result, its micrometre-scale single crystals can act as the efficient polarizer. Theoretical calculations proved that linear $(I_3)^-$ should be responsible for this giant optical anisotropy. Our work indicates that natural polyiodide crystals should be an excellent platform to develop compact and efficient polarizing optical devices for broad polarized photonic applications, such as optical communication, ultrahigh-resolution sensing and miniaturized photonic devices.

Online content

Any methods, additional references, Nature Portfolio reporting summaries, source data, extended data, supplementary information, acknowledgements, peer review information; details of author contributions and competing interests; and statements of data and code availability are available at https://doi.org/10.1038/s41566-024-01461-8.

References

1. Bartholin, R. *Experimenta crystalli Islandici disdiaclastici, quibus miraet insolita refractio detegitur*. (Daniel Paulli, 1669).
2. Bartholin, E. An accompt of sundry experiments made and communicated by that learn'd mathematician. *Philos. Trans. R. Soc. Lond.* **5**, 2139–2148 (1670).
3. Chen, X. et al. Solution-processed inorganic perovskite crystals as achromatic quarter-wave plates. *Nat. Photonics* **15**, 813–816 (2021).
4. Rubin, N. A. et al. Matrix Fourier optics enables a compact full-Stokes polarization camera. *Science* **365**, 1839–1846 (2019).
5. MacKenzie, L. E. & Pal, R. Circularly polarized lanthanide luminescence for advanced security inks. *Nat. Rev. Chem.* **5**, 109–124 (2021).
6. Ghosh, G. Dispersion-equation coefficients for the refractive index and birefringence of calcite and quartz crystals. *Opt. Commun.* **163**, 95–102 (1999).
7. Sinton, W. M. Birefringence of rutile in the infrared. *J. Opt. Soc. Am.* **51**, 1309–1310 (1961).
8. Luo, H. T., Tkaczyk, T., Dereniak, E. L., Oka, K. & Sampson, R. High birefringence of the yttrium vanadate crystal in the middle wavelength infrared. *Opt. Lett.* **31**, 616–618 (2006).
9. Zhou, G. Q. et al. Growth and spectrum of a novel birefringent α-BaB_2O_4 crystal. *J. Cryst. Growth* **191**, 517–519 (1998).
10. Tudi, A., Han, S. J., Yang, Z. H. & Pan, S. L. Potential optical functional crystals with large birefringence: recent advances and future prospects. *Coord. Chem. Rev.* **459**, 214380 (2022).
11. Sun, Y. et al. 3D-printed ferromagnetic liquid crystal elastomer with programmed dual-anisotropy and multi-responsiveness. *Adv. Mater.* **35**, 2302824 (2023).
12. Li, G. M., Yang, Z. H., Hou, X. L. & Pan, S. L. Chain-like $[S_x]$ (*x*=2–6) units realizing giant birefringence with transparency in the near-infrared for optoelectronic materials. *Angew. Chem. Int. Ed.* **62**, e202303711 (2023).

13. Niu, S. et al. Giant optical anisotropy in a quasi-one-dimensional crystal. *Nat. Photonics* **12**, 392–396 (2018).
14. Mei, H. et al. Colossal optical anisotropy from atomic-scale modulations. *Adv. Mater*. https://doi.org/10.1002/adma.202303588 (2023).
15. Xu, H. et al. Magnetically tunable and stable deep-ultraviolet birefringent optics using two-dimensional hexagonal boron nitride. *Nat. Nanotechnol*. **17**, 1091–1096 (2022).
16. Chen, S. et al. Real-space observation of ultraconfined in-plane anisotropic acoustic terahertz plasmon polaritons. *Nat. Mater.* **22**, 860–866 (2023).
17. Segura, A. et al. Natural optical anisotropy of h-BN: highest giant birefringence in a bulk crystal through the mid-infrared to ultraviolet range. *Phys. Rev. Mater.* **2**, 024001 (2018).
18. Ma, W. et al. In-plane anisotropic and ultra-low-loss polaritons in a natural van der Waals crystal. *Nature* **562**, 557–562 (2018).
19. Taboada-Gutierrez, J. et al. Broad spectral tuning of ultra-low-loss polaritons in a van der Waals crystal by intercalation. *Nat. Mater.* **19**, 964–969 (2020).
20. Gong, C. et al. Electronic and optoelectronic applications based on 2D novel anisotropic transition metal dichalcogenides. *Adv. Sci.* **4**, 1700231 (2017).
21. Wang, X. et al. Short-wave near-infrared linear dichroism of two-dimensional germanium selenide. *J. Am. Chem. Soc.* **139**, 14976–14982 (2017).
22. Song, H. et al. Highly anisotropic Sb_2Se_3 nanosheets: gentle exfoliation from the bulk precursors possessing 1D crystal structure. *Adv. Mater.* **29**, 1700441 (2017).
23. Long, M. et al. Room temperature high-detectivity mid-infrared photodetectors based on black arsenic phosphorus. *Sci. Adv.* **3**, e1700589 (2017).
24. Ermolaev, G. A. et al. Giant optical anisotropy in transition metal dichalcogenides for next-generation photonics. *Nat. Commun.* **12**, 854 (2021).
25. Dorrah, A. H., Rubin, N. A., Zaidi, A., Tamagnone, M. & Capasso, F. Metasurface optics for on-demand polarization transformations along the optical path. *Nat. Photon.* **15**, 287–296 (2021).
26. Dorrah, A. H. & Capasso, F. Tunable structured light with flat optics. *Science* **376**, eabi6860 (2022).
27. Svensson, P. H. & Kloo, L. Synthesis, structure, and bonding in polyiodide and metal iodide–iodine systems. *Chem. Rev.* **103**, 1649–1684 (2003).
28. Yang, S. D. et al. Polar phosphorus chalcogenide cage molecules: enhancement of nonlinear optical properties in adducts. *Angew. Chem. Int. Ed.* **62**, e202218272 (2023).
29. Song, B. et al. Broadband optical properties of graphene and HOPG investigated by spectroscopic mueller matrix ellipsometry. *Appl. Surf. Sci.* **439**, 1079–1087 (2018).
30. Gu, H. G., Chen, X. G., Jiang, H., Zhang, C. W. & Liu, S. Y. Optimal broadband Mueller matrixellipsometer using multi-waveplates with flexibly oriented axes. *J. Opt.* **18**, 025702 (2016).
31. Bai, Z. & Ok, K. M. Designing sulfate crystals with strong optical anisotropy through π-conjugated tailoring. *Angew. Chem. Int. Ed.* **63**, e202315311 (2023).
32. Zhang, X. et al. Finding the first squarates nonlinear optical crystal $NaHC_4O_4{\cdot}H_2O$ with strong second harmonic generation and giant birefringence. *ACS Materials Lett.* **4**, 572–576 (2022).
33. Zelmon, D. E., Small, D. L. & Jundt, D. Infrared corrected sellmeier coefficients for congruently grown lithium niobate and 5 mol.% magnesium oxide–doped lithium niobate. *J. Opt. Soc. Am. B* **14**, 3319–3322 (1997).
34. Zysset, B., Biaggio, I. & Günter, P. Refractive indices of orthorhombic $KNbO_3$. I. Dispersion and temperature dependence. *J. Opt. Soc. Am. B* **9**, 380–386 (1992).
35. Boyd, G. D., Kasper, H. & McFee, J. H. Linear and nonlinear optical properties of $AgGaS_2$, $CuGaS_2$, and $CuInS_2$, and theory of the wedge technique for the measurement of nonlinear coefficients. *IEEE J. Quantum. Elect.* **7**, 563–573 (1971).
36. Feng, Y. et al. Visible to mid-infrared giant in-plane optical anisotropy in ternary van der Waals crystals. *Nat. Commun.* **14**, 6739 (2023).
37. Xia, F., Wang, H. & Jia, Y. Rediscovering black phosphorus as an anisotropic layered material for optoelectronics and electronics. *Nat. Commun.* **5**, 4458 (2014).
38. Yu, J. et al. Direct observation of the linear dichroism transition in two-dimensional palladium diselenide. *Nano Lett.* **20**, 1172–1182 (2020).
39. Wu, J. et al. Linear dichroism conversion in quasi-1D perovskite chalcogenide. *Adv. Mater.* **31**, e1902118 (2019).
40. Lautenschlager, P., Garriga, M., Vina, L. & Cardona, M. Temperature-dependence of the dielectric function and interband critical-points in silicon. *Phys. Rev. B* **36**, 4821–4830 (1987).
41. Park, J. W. et al. Optical properties of pseudobinary GeTe,$Ge_2Sb_2Te_5$, $GeSb_2Te_4$, $GeSb_4Te_7$, andSb_2Te_3 from ellipsometry and density functional theory. *Phys. Rev. B* **80**, 115209 (2009).
42. Toyozawa, Y., Inoue, M., Inui, T., Okazaki, M. & Hanamura, E. Coexistence of local and band characters in the absorption spectra of solids I. Formulation. *J. Phys. Soc. Jpn* **22**, 1337–1349 (1967).
43. Guo, Z. et al. Complete dielectric tensor and giant optical anisotropy in quasi-one-dimensional $ZrTe_5$. *ACS Mater. Lett.* **3**, 525–534 (2021).
44. Savin, A., Nesper, R., Wengert, S. & Fässler, T. F. ELF: the electron localization function. *Angew. Chem. Int. Ed.* **36**, 1808–1832 (1997).

Methods

Materials

Hydroiodic acid (HI, 48%) and iodine (I_2) were obtained from Aladdin, and melamine ($C_3H_6N_6$) from Admas. All the chemicals were bought and used without further purification.

Synthesis

Crystals of $C_3H_8N_6I_6{\cdot}3H_2O$ were synthesized from the concentrated aqueous HI solutions. Firstly, $C_3H_6N_6$ was mixed with 48% HI aqueous solution in a molar ratio of 1:2, followed by heating the mixture with continuous stirring up to 50 °C until a clear solution was obtained. Subsequently, iodine (the molar ratio with $C_3H_6N_6$ is 1:1) was added to the hot solution. Then, the reaction mixture was thoroughly stirred with heating under 50 °C thoroughly. Finally, large-sized crystals were grown slowly at a cooling rate of 1 °C per day.

Single-crystal XRD

Single-crystal XRD data for $C_3H_8N_6I_6{\cdot}3H_2O$ were collected by graphite-monochromatized Mo Kα radiation (λ = 0.7107 Å) on an Agilent Bruker D8 diffractometer at 100 K. More details can be found in single-crystal structure of Supplementary Information S2.

Powder XRD

Powder XRD patterns were obtained from the powder XRD analysis and performed on a Miniflex600 diffractometer equipped with Cu Kα radiation at room temperature.

HRTEM

The HRTEM with electron diffraction spectroscopy (Titan G2 60-300) was used to identify the quality of $C_3H_8N_6I_6{\cdot}3H_2O$ crystal.

LIDT

The LIDT was evaluated on a 1,064 nm Nd. YAG laser using the r-on-1 technique. The LIDT of $C_3H_8N_6I_6{\cdot}3H_2O$ was measured with a sample size of 4 × 4 × 2 mm^3. The crystal was irradiated using single-pulse energy, and then the pulse energy was increased until irreversible damage was observed on the sample surface.

Hardness test

The hardness test was performed with a Vickers hardness tester, in which the load of the tetragonal diamond indenter was 0.49 N for 15 s, and the diagonal length of the indentation was 310 μm and 357 μm, respectively.

UV–vis–NIR diffuse transmission spectrum

UV–vis–NIR diffuse transmittance spectra were obtained on a Perkin-Elmer Lambda 950 UV–vis–IR spectrophotometer.

Mueller matrix spectroscopic ellipsometry measurement and analysis

Mueller matrix spectra were utilized to detect the polarization state changes of optically anisotropic $C_3H_8N_6I_6{\cdot}3H_2O$, collected by a commercial Mueller matrix spectroscopic ellipsometer (ME-L Muller matrix ellipsometer, Wuhan E-optics Technology). The instrument was used to acquire Mueller matrix spectra. As illustrated in Supplementary Fig. 7, we changed the azimuthal angle of the ellipsometry (defined as the angle between the *a* axis and the *y* axis of the ellipsometric coordinates of $C_3H_8N_6I_6{\cdot}3H_2O$) in our experiments by rotating the samples in the *a*–*c* plane. Spectroscopic data were obtained in the spectral range of 200–1,690 nm with a 200 μm probing spot and incident angles of 60°, 65° and 70°. The ellipsometric analysis is a model-based method. The optical model was constructed to obtain calculated Mueller matrix spectra, and then the calculated Mueller matrix spectra were used to fit with the measured ones by adjusting and optimizing the parameters of the optical model[43,45]. The reflected light passes through an objective and is directed onto a charge-coupled Device (CCD) camera in the microscope configuration. The complete dielectric tensor of $C_3H_8N_6I_6{\cdot}3H_2O$ is obtained with a 200 μm probing spot. Spectroscopic data are obtained in the spectral range of 200–1,690 nm. $C_3H_8N_6I_6{\cdot}3H_2O$ has a 3 × 3 matrix of dielectric tensor matrix, where the diagonal elements are approximated by the dielectric function ε ($\varepsilon = \varepsilon_r - i\varepsilon_i$, where ε_r and ε_i are real parts and imaginary parts of ε, respectively along the *x* axis, *y* axis and *z* axis of ellipsometric coordinate. More details can be found in the Mueller Matrix Spectroscopic Ellipsometry measurement and analysis of Supplementary Information S3.

CP analysis

CP analysis was used to demystify the underlying relationship between the structure and optical performance of $C_3H_8N_6I_6{\cdot}3H_2O$. In brief, the characteristic peaks in dielectric function ε can be recognized as the CPs with different types and parameters. By combining the CP analysis results with the first-principles calculations, the CPs correspond to the interband transition of carriers in the band structure and partial DOS[40]. More details can be found in the CP Analysis of Supplementary Information S4.

Visualized optical anisotropy tests

The single crystals of $C_3H_8N_6I_6{\cdot}3H_2O$ were characterized by the polarized method under the polarized microscope (Nikon ECLIPSE LV100N POL). The alignment of the crystal on the goniometer was carried out by visual inspection, with the long axis of the needle morphology (*a* axis) aligned parallel to the direction of polarized light. The changes in brightness and darkness of a crystal were observed by rotating the object stage.

Computational methods

The CASTEP package implemented the plane-wave pseudopotential method for first-principles calculations based on density functional theory[46]. See Supplementary Information S5 for more details.

Data availability

The authors declare that all data supplementary to the findings of this study are available within the paper and its Supplementary Information files. The X-ray crystallographic coordinates for structure reported in this study has been deposited at the Cambridge Crystallographic Data Centre (CCDC), under deposition number 2151897. These data can be obtained free of charge from The Cambridge Crystallographic Data Centre via www.ccdc.cam.ac.uk/data_request/cif. Any further relevant data are available from the authors upon reasonable request.

References

45. Liu, S., Chen, X. & Zhang, C. Development of a broadband Mueller matrix ellipsometer as a powerful tool for nanostructure metrology. *Thin Solid Films* **584**, 176–185 (2015).
46. Medvedev, M. G., Bushmarinov, I. S., Sun, J., Perdew, J. P. & Lyssenko, K. A. Density functional theory is straying from the path toward the exact functional. *Science* **355**, 49–52 (2017).

Acknowledgements

We thank S. G. Zhao, J. H. Luo, and H. G. Gu for helpful discussions and experimental assistance. This work acknowledges the financial support from the National Natural Science Foundation of China (22122507 (S.Z.), 22193042 (J.L.) and 21921001 (J.L.)), Guangdong Basic and Applied Basic Research Foundation (grant no. 2023A1515030149) (H.G.), the Natural Science Foundation of Fujian Province (2022J02012) (S.Z.), the Youth Innovation Promotion Association of Chinese Academy of Sciences (Y202069) (S.Z.)

and the Key Research Program of Frontier Sciences of the Chinese Academy of Sciences (ZDBS-LY SLH024) (J.L.).

Author contributions

S.Z. and J.L. contributed to the conception of the research. M.H. provided suggestions for research. H.G. and S.L. guided and Z.G. performed the Mueller matrix spectroscopic ellipsometry analyses and CP analyses. Y.Z. performed the experiments and wrote the manuscript. Y.L., X.Z. and Y.S. assisted in the experimental and theoretical analysis. All authors discussed the results and reviewed the manuscript.

Competing interests

The authors declare no competing interests.

Additional information

Supplementary information The online version contains supplementary material available at https://doi.org/10.1038/s41566-024-01461-8.

Correspondence and requests for materials should be addressed to Honggang Gu, Sangen Zhao or Junhua Luo.

Peer review information *Nature Photonics* thanks Kang Min Ok, Bingbing Zhang and the other, anonymous, reviewer(s) for their contribution to the peer review of this work.

nature photonics

Supplementary information

https://doi.org/10.1038/s41566-024-01461-8

A solution-processable natural crystal with giant optical anisotropy for efficient manipulation of light polarization

In the format provided by the authors and unedited

CONTENTS

S1 The Birefringence of some Van Der Waals Layered Materials

Supplementary Table 1. The in-plane and out-plane birefringence of typical van der Waals layered materials.

No.	Formula	In-plane birefringence	Out-plane birefringence (Δn)	Ref.
1	h-BN	0	−0.7 in the visible to −2 in the deep ultraviolet	[1]
2	MoS_2	0	1.5 in the infrared and 3 in the visible light	[2]
3	BP	0	0.23@520 nm	[3]
4	ReS_2	0.037@520 nm	/	[4]
5	$ReSe_2$	0.047@520 nm	/	[4]

S2 Single-Crystal Structure Determination

Single crystal X-ray diffraction data for $C_3H_8N_6I_6 \cdot 3H_2O$ was collected under graphite-monochromatized Mo Kα radiation (λ = 0.7107Å) at 100 K on an Agilent Bruker D8 diffractometer. We used the program APEX3 for Data integration, cell refinement and absorption corrections. The crystal structure of $C_3H_8N_6I_6 \cdot 3H_2O$ was solved by using the directed methods, and then refined by full-matrix least-squares fitting on F^2 using SHELXL on OLEX2 package[5,6]. The PLATON[7] program was used to check for the structure, and no higher symmetry was found. Crystallographic data and structure refinements of $C_3H_8N_6I_6 \cdot 3H_2O$ were given in the Table S2. Atomic coordinates, equivalent isotropic displacement parameters, selected bond lengths and angles, and anisotropic displacement parameters for $C_3H_8N_6I_6 \cdot 3H_2O$ were shown in Table S3-S5.

Supplementary Table 2. Crystal data and structure refinement for $C_3H_8N_6I_6 \cdot 3H_2O$.

Formula sum	$C_3H_8N_6I_6 \cdot 3H_2O$
Formula weight (g/mol)	1887.22
Crystal color	Dark
Crystal system	monoclinic
Space group	$P2_1/n$
a/Å	9.48715(13)
b/Å	27.2664(3)
c/Å	14.9897(2)
α/°	90
β/°	97.9031(13)
γ/°	90
V/Å^3	3840.70(9)
Z	4
$\rho_{(calc)}$ (g/cm^3)	3.2635
μ/mm^{-1}	52.481
F(000)	3339.6
Data/restraints/parameters	6787/4/342
Index ranges	-12≤h≤11, -34≤k≤35, -19≤l≤19
R(int)	0.0647
GOF(F^2)	1.038
Reflections collected	32154
Final R indexes [I>=2σ (I)]	R_1 = 0.0571, wR_2 = 0.1652
Final R indexes [all data]	R_1 = 0.0598, wR_2 = 0.1694

[a] $R_1 = \sum ||F_o| - |F_c|| / \sum |F_o|$ and $wR_2 = [\sum [w(F_o^2 - F_c^2)^2] / [\sum [w(F_o^2)^2]]1/2$ for $F_o^2 > 2\sigma(F_c^2)$

Supplementary Table 3. Fractional atomic coordinates ($\times 10^4$) and equivalent isotropic displacement parameters ($Å^2 \times 10^3$) for $C_3H_8N_6I_6 \cdot 3H_2O$.

Atom	*x/a*	*y/b*	*z/c*	*U*(eq)
I1	6527.6(6)	3063.9(2)	9855.8(3)	36.53(18)
I2	832.3(6)	2146.7(2)	7619.7(3)	37.90(18)
I3	1269.8(6)	4505.9(2)	6079.3(3)	37.65(19)
I4	9695.4(6)	3118.0(2)	9816.1(3)	39.15(19)
I5	3970.8(6)	2062.73(19)	7555.6(4)	37.35(19)
I6	6266.2(6)	5431.70(19)	1189.5(3)	37.06(19)
I7	4291.3(6)	4554.07(19)	6051.6(3)	38.44(19)
I8	3519.6(7)	3035.9(2)	9872.4(3)	39.01(18)
I9	9491.6(6)	5435.0(2)	1118.6(4)	40.37(19)
I10	-1865.7(6)	4457.7(2)	6154.0(4)	40.23(18)
I11	6984.3(7)	2040.8(2)	7509.7(4)	40.97(19)
I12	3295.5(7)	5413.1(2)	1221.9(4)	40.35(19)
O1	-517(7)	3119(2)	6007(4)	41.7(13)
O2	1538(7)	3460(2)	7673(4)	42.0(14)
O3	1980(8)	4096(3)	1083(5)	50.6(16)
O4	7969(7)	3441(2)	7619(4)	45.1(14)
O5	8488(7)	4150(2)	1060(4)	47.3(15)
O6	501(7)	4379(2)	2766(4)	45.6(14)
N1	5644(8)	3267(2)	6362(4)	39.0(15)
N2	4673(8)	3403(3)	7657(4)	38.0(16)
N3	5320(8)	4121(3)	1041(5)	42.3(17)
N4	3205(7)	3300(2)	6308(4)	36.5(15)
N5	6615(8)	3159(3)	5045(5)	42.0(16)
N6	4320(8)	4160(3)	2355(4)	38.4(15)

Atom	*x/a*	*y/b*	*z/c*	*U*(eq)
N7	8189(8)	4136(3)	3791(5)	41.0(16)
N8	3351(7)	4207(3)	3675(5)	39.9(16)
N9	6758(8)	4152(2)	2419(4)	39.1(15)
N10	4185(8)	3226(2)	4943(4)	38.8(15)
N11	1780(8)	3277(3)	4933(4)	39.6(15)
N12	5758(8)	4138(3)	3772(4)	41.1(16)
C1	3075(9)	3263(3)	5390(5)	38.9(18)
C2	4514(10)	3327(3)	6788(5)	40.4(18)
C3	5457(10)	4142(3)	1933(5)	40.9(19)
C4	6870(10)	4141(3)	3349(5)	39.8(19)
C5	4475(9)	4170(3)	3279(5)	37.6(18)
C6	5459(10)	3213(3)	5430(5)	36.9(18)

[a]U_{eq} is defined as 1/3 of the trace of the orthogonalised U_{ij} tensor.

Supplementary Table 4. Anisotropic displacement parameters ($Å^2×10^3$) for $C_3H_8N_6I_6·3H_2O$.

Atom	U_{11}	U_{22}	U_{33}	U_{23}	U_{13}	U_{12}
I1	47.6(4)	30.9(3)	30.4(3)	-0.4(2)	3.1(2)	0.52(19)
I2	47.6(3)	32.6(3)	32.9(3)	0.5(2)	3.6(2)	0.6(2)
I3	51.4(4)	29.8(3)	31.1(3)	0.9(2)	3.4(2)	0.7(2)
I4	46.4(3)	35.9(3)	34.5(3)	0.1(2)	3.4(2)	-1.0(2)
I5	49.9(4)	30.2(3)	31.2(3)	0.0(2)	2.9(3)	0.3(2)
I6	48.9(4)	31.3(3)	30.2(3)	-0.8(2)	2.8(2)	-0.70(19)
I7	48.9(3)	31.2(3)	35.0(3)	-0.9(2)	5.0(2)	0.3(2)
I8	46.6(3)	35.9(3)	33.9(3)	-2.3(2)	3.3(2)	1.2(2)
I9	47.9(3)	37.3(3)	35.4(3)	-0.9(2)	3.9(2)	-0.2(2)
I10	48.0(3)	37.2(3)	34.9(3)	-1.1(2)	3.6(2)	-0.5(2)
I11	48.6(4)	38.4(3)	35.2(3)	2.2(2)	3.0(2)	1.4(2)
I12	48.4(4)	36.2(3)	35.9(3)	-0.2(2)	3.8(2)	-1.8(2)
O1	48(3)	38(3)	37(3)	4(3)	1(3)	-5(2)
O2	57(4)	35(3)	34(3)	-4(3)	7(3)	4(3)
O3	60(4)	40(4)	48(4)	-3(3)	-7(3)	-1(3)
O4	59(4)	37(3)	36(3)	-3(3)	-3(3)	5(3)
O5	62(4)	38(4)	43(3)	-4(3)	11(3)	-6(3)
O6	60(4)	39(3)	37(3)	-1(3)	4(3)	-2(3)
N1	53(4)	30(3)	33(3)	7(3)	-1(3)	-3(3)
N2	53(4)	31(4)	28(3)	2(3)	-3(3)	1(3)
N3	53(4)	40(4)	32(4)	2(3)	0(3)	-3(3)
N4	40(4)	31(3)	37(3)	-3(3)	5(3)	1(3)
N5	49(4)	45(4)	30(3)	7(3)	0(3)	0(3)
N6	44(4)	35(4)	34(3)	2(3)	-2(3)	-1(3)

Atom	U_{11}	U_{22}	U_{33}	U_{23}	U_{13}	U_{12}
N7	46(4)	46(4)	29(3)	3(3)	-3(3)	-3(3)
N8	42(4)	42(4)	36(4)	-4(3)	5(3)	0(3)
N9	52(4)	32(3)	32(3)	-3(3)	2(3)	1(3)
N10	50(4)	34(4)	29(3)	6(3)	-5(3)	5(3)
N11	47(4)	42(4)	28(3)	-2(3)	-1(3)	-4(3)
N12	56(5)	35(4)	31(3)	1(3)	2(3)	0(3)
C1	50(5)	27(4)	36(4)	2(3)	-3(4)	-1(3)
C2	55(5)	28(4)	37(4)	5(4)	3(4)	3(3)
C3	59(5)	27(4)	38(4)	-4(4)	9(4)	4(3)
C4	55(5)	29(4)	32(4)	9(4)	-5(4)	-3(3)
C5	52(5)	27(4)	32(4)	-2(3)	0(4)	5(3)
C6	54(5)	27(4)	28(4)	3(3)	3(4)	3(3)

Supplementary Table 5. Selected bond distances (Å) and angles (deg.) for $C_3H_8N_6I_6 \cdot 3H_2O$.

I1—I4	3.0177(7)	N4—C1	1.349(11)
I1—I8	2.8583(8)	N5—C6	1.315(11)
I2—I5	3.0010(8)	N6—C3	1.324(11)
I3—I7	2.8755(8)	N6—C5	1.372(10)
I3—I10	2.9951(8)	N7—C4	1.333(11)
I5—I11	2.8699(8)	N8—C5	1.294(11)
I6—I9	3.0764(8)	N9—C3	1.344(12)
I6—I12	2.8259(8)	N9—C4	1.385(10)
N1—C2	1.331(11)	N10—C1	1.326(11)
N1—C6	1.392(10)	N10—C6	1.324(11)
N2—C2	1.307(11)	N11—C1	1.323(11)
N3—C3	1.327(11)	N12—C4	1.304(11)
N4—C1	1.369(10)	N12—C5	1.337(11)
I8—I1—I4	178.59(2)	N4—C2—N1	118.7(7)
I10—I3—I7	178.69(2)	N4—C2—N2	120.7(8)
I11—I5—I2	176.78(2)	N6—C3—N3	120.7(8)
I12—I6—I9	178.69(2)	N9—C3—N3	120.1(8)
C6—N1—C2	119.7(8)	N9—C3—N6	119.2(7)
C2—N4—C1	119.3(7)	N9—C4—N7	116.0(8)
C5—N6—C3	120.1(7)	N12—C4—N7	121.7(8)
C4—N9—C3	118.9(7)	N12—C4—N9	122.3(8)
C6—N10—C1	116.9(7)	N8—C5—N6	118.9(8)
C5—N12—C4	117.8(7)	N12—C5—N6	121.3(8)
N10—C1—N4	123.0(7)	N12—C5—N8	119.8(7)
N11—C1—N4	117.9(8)	N5—C6—N1	117.0(8)
N11—C1—N10	119.1(7)	N10—C6—N1	122.0(8)
N2—C2—N1	120.5(8)	N10—C6—N5	121.0(7)

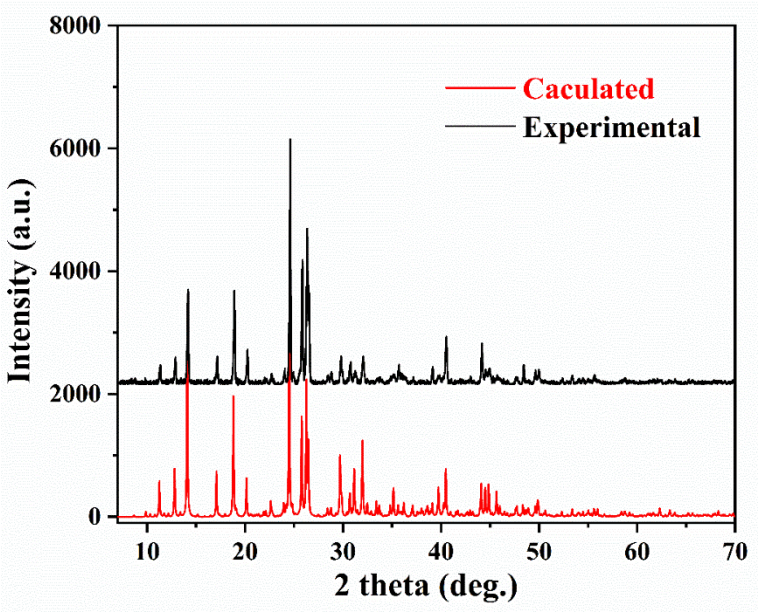

Supplementary Fig. 1 The powder X-ray diffraction patterns of $C_3H_8N_6I_6 \cdot 3H_2O$.

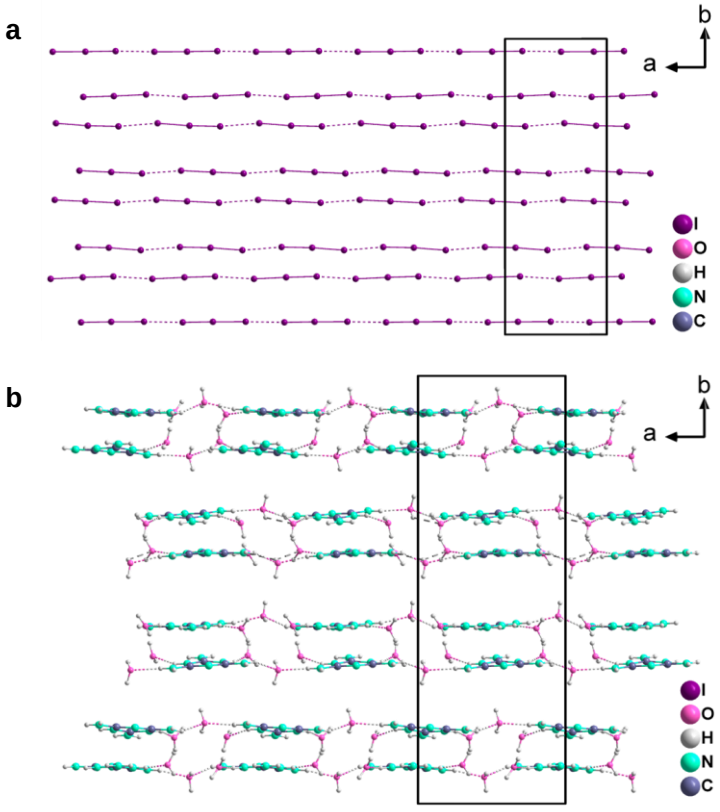

Supplementary Fig. 2 (a) Detailed structure of polyiodide chain packing along *a* axis. (b) The $(C_3H_8N_6)^{2+}$ cation packing along *a* axis.

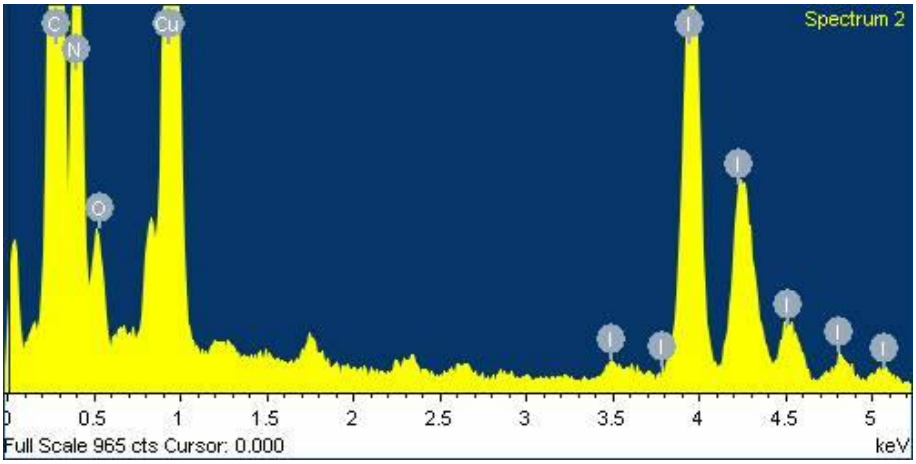

Supplementary Fig. 3 The EDS spectrum of $C_3H_8N_6I_6 \cdot 3H_2O$ crystal.

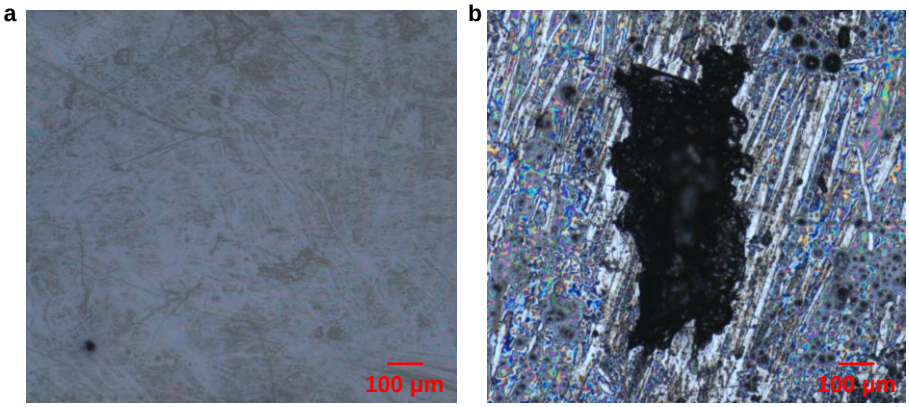

Supplementary Fig. 4 Photograph of the $C_3H_8N_6I_6 \cdot 3H_2O$ crystal surface before (a) and after (a) laser damage under an optical microscope. Scale bar: 100 μm.

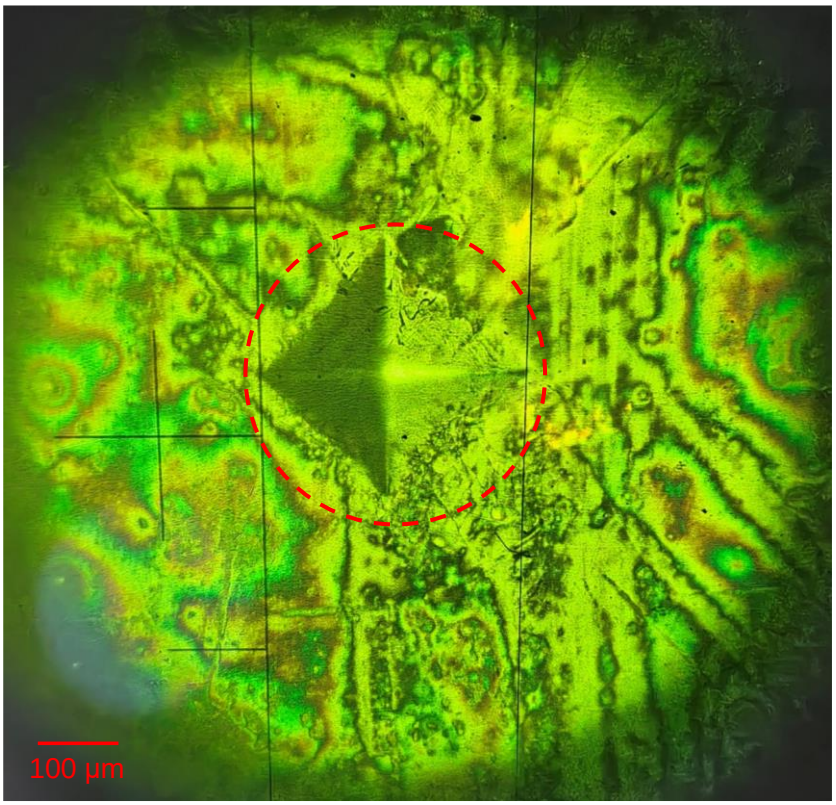

Supplementary Fig. 5 A clear indentation pit produced by a diamond square cone indenter pressed into the surface of $C_3H_8N_6I_6 \cdot 3H_2O$ crystal. Scale bar: 100 μm.

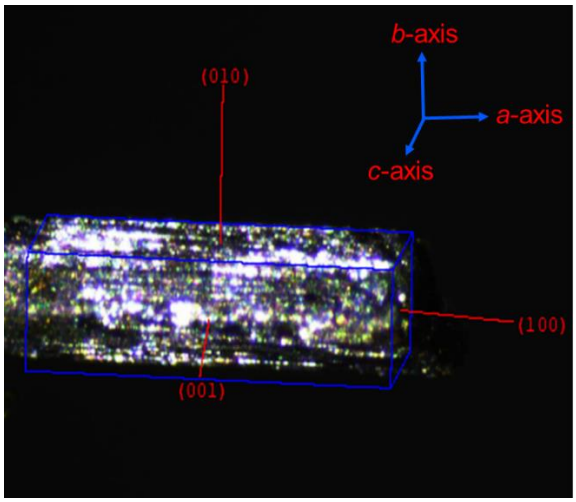

Supplementary Fig. 6 The $C_3H_8N_6I_6 \cdot 3H_2O$ crystal faces are determined by Agilent Bruker D8 diffractometer.

S3 Mueller Matrix Spectroscopic Ellipsometry Measurement and Analysis

Ellipsometric analysis is a model-based method. The optical model is constructed to obtain calculated Mueller matrix spectra, and then the calculated Mueller matrix spectra is used to fit with the measured ones by adjusting and optimizing the parameters of the optical model. In the Mueller matrix spectroscopic ellipsometry measurements, the linearly polarized light is generated by a linear polarizer and modulated by a rotating compensator. The continuously modulated polarized light is illuminated on the $C_3H_8N_6I_6 \cdot 3H_2O$ sample and then reflected after incorporating the optical information of the sample. The polarized light reflected from the sample is further demodulated by a second rotating compensator followed by another linear polarizer (usually known as the analyzer) and finally detected by a spectrometer. The first and the second compensators are rotated synchronously by hollow servo motors with an angular velocity ratio of 5:3. By detecting and analyzing the modulated light intensity, the Mueller matrix of the sample can be obtained, which contains abundant information, especially including the optical anisotropy, about the sample. The synchronization controller and data acquisition system are connected to a computer, which is also responsible for the data processing. The measurement can be performed at different incident angles in the range of 45~90° and azimuthal angles in the range of 0-360° by rotating the two arms of the Mueller matrix and the sample stage with six degrees of freedom, respectively. By performing ellipsometric analysis, the optical information such as anisotropic refractive indices and extinction coefficients of the sample can be extracted from the measured Mueller matrix[8,9].

In the firstly isotropic ellipsometric analysis, B-spline fitting is parameterized by Lorentz oscillators and Tauc-Lorentz oscillators to constitute the dielectric function ε. The dielectric function ε is used to fit ellipsometric parameters (the amplitude ratio ψ and the phase difference Δ of *p*- and *s*-polarized light). Then the isotropic oscillators models are converted to biaxial anisotropic model. The biaxial anisotropic model originated from the dielectric functions ε along three directions of ellipsometric coordinate aixs (*x*-, *y*-, and *z*-axis), namely ε_x, ε_y, and ε_z, to fit the Mueller matrix. Herein, the dielectric functions ε_k ($k = x$ and z) can be expressed as follows[10]:

$$\varepsilon_{\mathrm{k}} = \sum_{q}^{Q} \varepsilon_{\text{Tauc-Lorentz}}^{q}(A_{\mathrm{q}}, \eta_q, E_{0,\,q}, E_{\mathrm{g},\,q}; E), \tag{1}$$

where $\varepsilon_{\text{Tauc-Lorentz}}^{q}$ is the qth Tauc-Lorentz oscillator model. They can be respectively written as

$$\varepsilon^{q}_{\text{Tauc-Lorentz}}(E) = \varepsilon_{\text{r},\,q} - \text{i}\varepsilon_{\text{i},\,q}, \quad (2a)$$

$$\varepsilon_{\text{i},\,q}(E) = \begin{cases} \dfrac{A_q \eta_q E_{0,\,q}(E - E_{\text{g},\,q})^2}{(E^2 - E_{0,\,q}^2)^2 + \eta_q^2 E^2} \cdot \dfrac{1}{E}; & E > E_{\text{g},\,q} \\ 0. & E \le E_{\text{g},\,q} \end{cases} \quad (2b)$$

In **Equation 2a**, $\varepsilon_{\text{r},\,q}$ and $\varepsilon_{\text{i},\,q}$ are respectively the real and imaginary part of dielectric functions for Tauc-Lorentz oscillator model. In Equation 2b, A_q, η_q, $E_{0,\,q}$, and $E_{\text{g},\,q}$ refer to the qth Tauc-Lorentz oscillator's amplitude, the damping coefficient, the center energy of the oscillators, and the bandgap energy respectively. $\varepsilon_{\text{r},\,q}$ can be obtained by Kramers–Kronig relation, which describes the relation between the real part and imaginary part of dielectric functions[8]

$$\varepsilon_{\text{r},q}(\text{E}) = \varepsilon_{\text{r},q}(\infty) + \frac{2}{\pi} P \int_{E_{\text{g},q}}^{\infty} \frac{\xi \varepsilon_{\text{i},q}(\xi)}{\xi^2 - \text{E}^2} d\xi, \quad (3)$$

where $\varepsilon_{\text{r,q}}(\infty)$ is an additional fitting parameter and P is the Cauchy principal value of the integral.

The Cauchy model fit well with the dielectric function along y-axis ε_y instead of Tauc-Lorentz oscillators. The Cauchy model is defined by Cauchy dispersion equations in the form of refractive index n_y and extinction coefficient k_y is zero[8]:

$$n_{\text{z}}(E) = \text{A} + \text{B}E^2 + \text{C}E^4, \quad (4)$$

where A, B, and C represent the analytical parameters of the Cauchy dispersion equations.

In ellipsometric analysis of $C_3H_8N_6I_6 \cdot 3H_2O$, five and four Tauc-Lorentz oscillators make up the imaginary part of the $\varepsilon_{\text{i},\,x}$ and $\varepsilon_{\text{i},\,z}$, respectively. All the best fitted parameters of oscillators are listed in Supplementary Table 6. In y-direction, analytical parameters A, B, and C of the well-fitted Cauchy model are 2.08, 7.74×10^{-2}, and 2.78×10^{-3}, respectively.

Supplementary Table 6. The best fitted parameters of oscillators model along *x*- and *z*-axis.

	Center energy (E_0) [eV]	Bandgap energy (E_g) [eV]	Amplitude (A) [eV]	Damping coefficient (η) [eV]
$\varepsilon_{i,\,x}$	0.04	0.004	86.68	0.17
	0.60	1.26	19.31	0.69
	2.00	0.29	17.90	0.54
	3.47	0.36	9.57	-*
	6.58	2.12	3.17	0.82
$\varepsilon_{i,\,z}$	0.51	4.19	1.13	37.35
	7.56	0.11	3.00	2.95
	9.32	2.50	24.29	5.90
	10.40	0	1.46	22.36

*Although this damping coefficient is out of range, we still adopt this oscillator since other parameters of this oscillator show great influence in fitting the imaginary part of the $\varepsilon_{i,x}$.

The Euler angles φ and θ are fitted to make (part of) crystal axes parallel to the ellipsometric coordinate axes, and the samples with different azimuths is conducted to multi sample analysis to determine reasonable Euler angle φ. Herein, the samples with azimuths of 0°, 30°, 45° and 90° are respectively best fitted with Euler angle φ of 0.02°, 30.68°, 45.96° and 95.76°, which probably means that one of the crystal axes of $C_3H_8N_6I_6{\cdot}3H_2O$ is parallel to *x*-axis of ellipsometric coordinate. Besides, the Euler angle θ is always −71.64° in multi sample analysis.

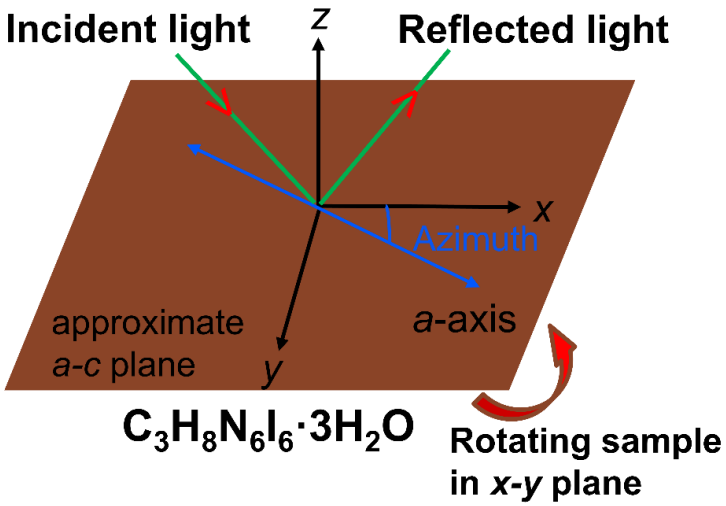

Supplementary Fig. 7 Schematic diagram of $C_3H_8N_6I_6 \cdot 3H_2O$ measurement by Mueller matrix spectroscopic ellipsometry, where the azimuth is defined as the angle between the *a*-axis and the *y*-axis.

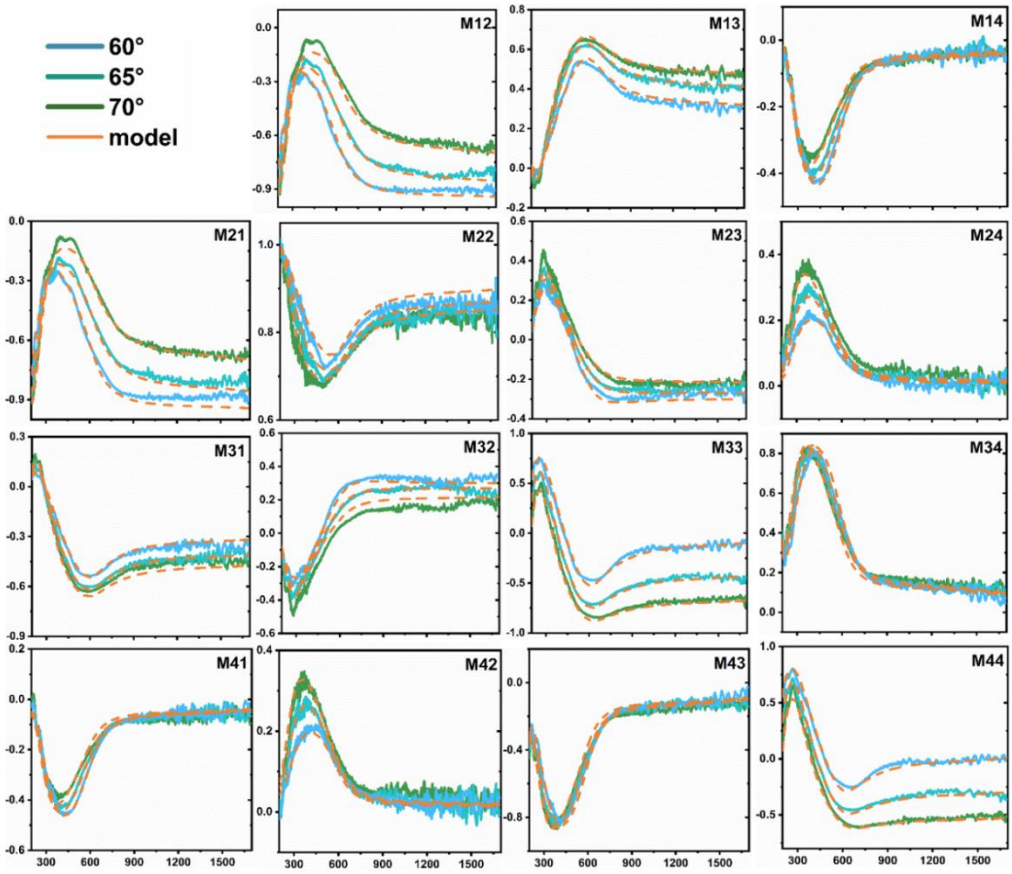

Supplementary Fig. 8 Mueller matrix spectra with incident angle θ from 60° to 70° and the best fitted curves of $C_3H_8N_6I_6 \cdot 3H_2O$ crystal.

The dielectric functions and the complex refractive index N can be mutually converted by the following

$$\varepsilon = N^2 \quad (5)$$

$$N = n - ik \quad (6)$$

With the complex refractive index, the reflectance R can be calculated theoretically according to[4]:

$$R_x = \frac{(n_x-1)^2+k_x^2}{(n_x+1)^2+k_x^2} \quad (7)$$

Here, the subscript x refers to *x*, *y*, or z, respectively, denoting physical quantities (*R*, *n*, and *k*) along *x*-, *y*-, and *z*-axes of ellipsometric coordinate, respectively.

$$\alpha_x = 4\pi k_x/\lambda \quad (8)$$

Here, the subscript x refers to *x*, *y*, or *z*, respectively, denoting physical quantities (α, *n*, and *k*) along *x*-, *y*-, and *z*-axes of ellipsometric coordinates, respectively.

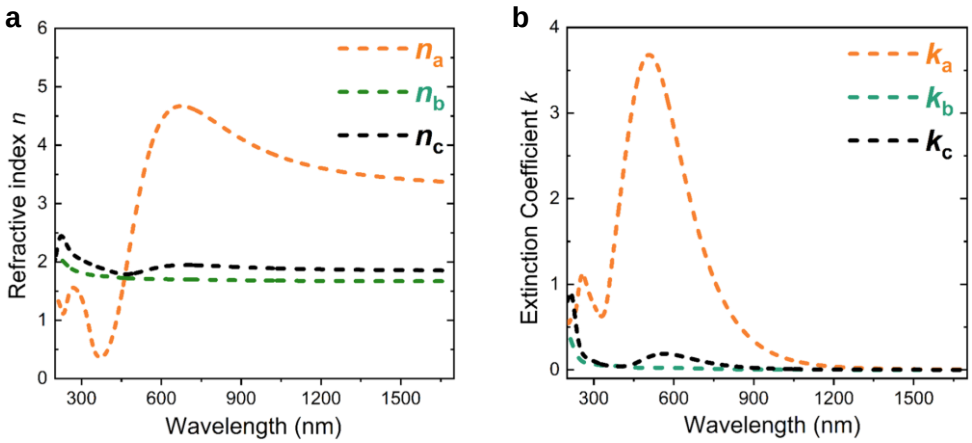

Supplementary Fig. 9 The refractive index (a) and extinction coefficient (b) of $C_3H_8N_6I_6 \cdot 3H_2O$ along *a*-axis, *b*-axis, and *c*-axis based on the first-principles calculations.

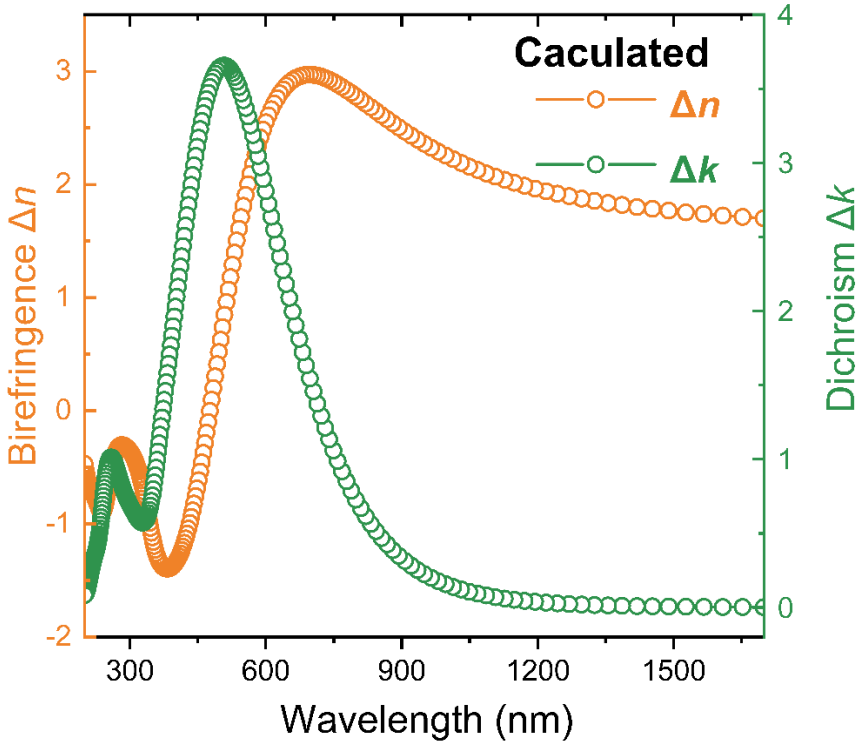

Supplementary Fig. 10 Birefringence and dichroism of $C_3H_8N_6I_6{\cdot}3H_2O$ calculated by the first-principles.

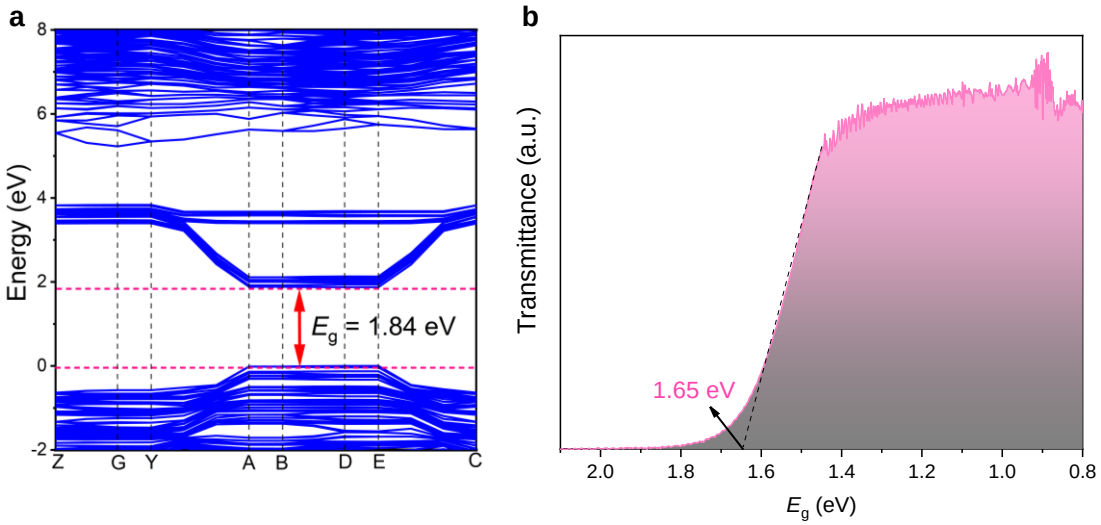

Supplementary Fig. 11 (a) The electronic band structure of $C_3H_8N_6I_6{\cdot}3H_2O$. (b) The transmission spectrum of $C_3H_8N_6I_6{\cdot}3H_2O$.

S4 Critical Point (CP) Analysis

The second derivative of dielectric functions expressed as the form of CPs is following[11]:

$$\frac{d^2\varepsilon}{dE^2} = \begin{cases} m(m-1)Ae^{i\Phi}((E-E_0+i\Gamma)^{m-2} & m \neq 0 \\ Ae^{i\Phi}((E-E_0+i\Gamma)^{-2}, & m = 0 \end{cases} \quad (9)$$

where A is the amplitude, Φ is the phase angle, E_0 is the center energy, and Γ is the broadening of the peak. The exponent m = 1/2, 0, and 1/2 respectively correspond to the three-dimensional, the two-dimensional, and the one-dimensional CPs. A discretely excitonic line shape (zero-dimensional CPs), resulting from the interaction of the discrete excitation with a continuous background[12], corresponds to m = -1. The best fitted parameters (A, Φ, E_0 and Γ) are listed in Table S6, and the $d^2\varepsilon/dE^2$ of the $C_3H_8N_6I_6 \cdot 3H_2O$ matches the discretely excitonic CPs best, i.e. m = -1. Here, we identify the transition at CPs by the following steps. (1) equal-energy lines (EELs) are drawn throughout the CPs and E_{C-V} subfigures according to the center energies of CPs. The tangent points between EELs and E_{C-V} curves can be regarded as transition positions. (2) Equal-momentum lines (EMLs) are drawn throughout the E_{C-V} and the band structure subfigures to distinguish the energy bands involved in the transitions of CPs. (3) EELs are drawn throughout the band structure and partial DOS subfigures to figure out the specific carrier types responsible for the transitions. The interband transitions are along *x*- and *z*-axis in the concerned energy region.

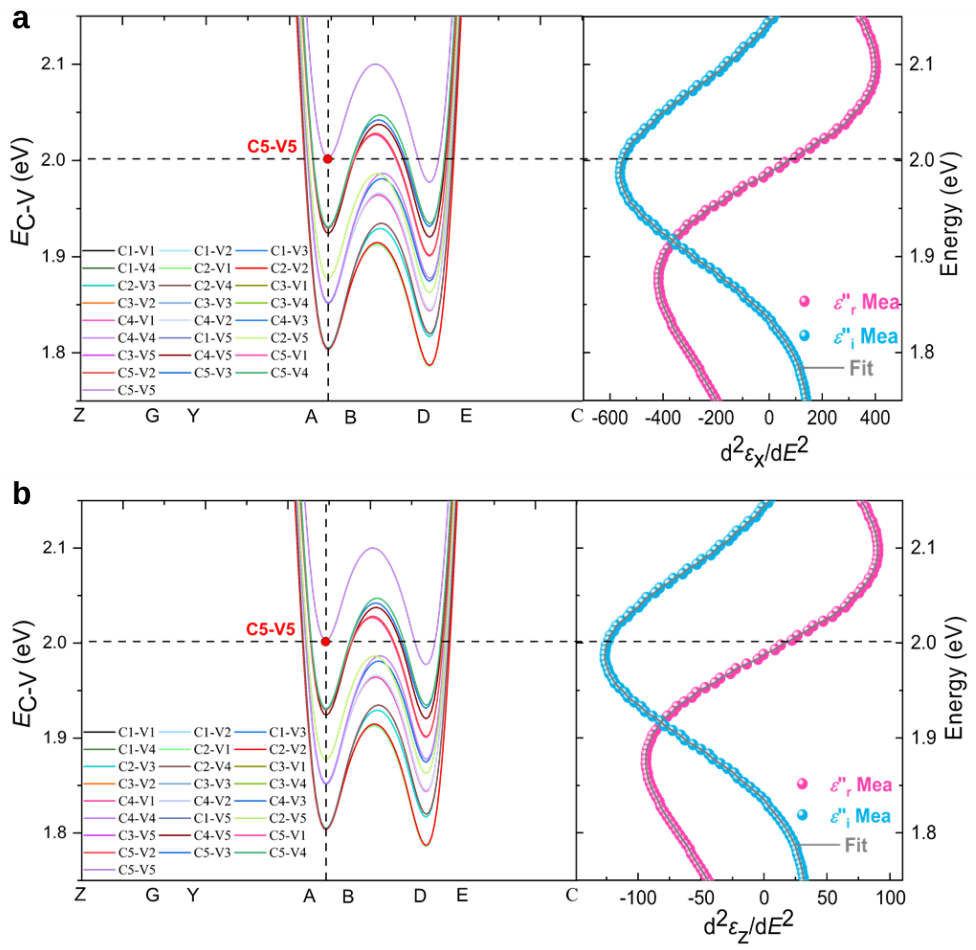

Supplementary Fig. 12 (a) Energy differences E_{C-V} between the first four CBs and the first four VBs of monolayer $C_3H_8N_6I_6 \cdot 3H_2O$. (b) CP analysis result of $C_3H_8N_6I_6 \cdot 3H_2O$ in the range of 1.75-2.15 eV.

Supplementary Table 7. The best fitted parameters for CPs of $C_3H_8N_6I_6 \cdot 3H_2O$.

	Center energy (E_0) [eV]	Phase angle (Φ)[°]	Amplitude (A) [F/m]	Broadening (Γ) [eV]
$d^2\varepsilon_x/dE^2$	2.0	179.02	5.43	0.27
$d^2\varepsilon_z/dE^2$	2.0	84.77	1.22	0.27

S5 Computational Methods

Based on the density functional theory (DFT) method[13], the band structure of $C_3H_8N_6I_6 \cdot 3H_2O$ was calculation by using CASTEP[14] code in the Material Studio package. The exchange and correlative potential of electron-electron interactions was treated by using the generalized gradient approximation (GGA) in the scheme of Perdew-Burke-Ernzerhof (PBE)[15], Due to the discontinuity of exchange-correlation energy, the calculated results are smaller than the experimental observations, the energy band gap was calculated by the scissors-corrected PBE method[16] where the scissors operator was set as 0.5. The following orbital electrons were regarded as the valence electrons: C $2s^2 2p^2$; N $2s^2 2p^3$; O $2s^2 2p^4$; I $5s^2 5p^5$; H $1s^1$. In addition, the energy cutoff of $C_3H_8N_6I_6 \cdot 3H_2O$ was chosen as 750 eV and the k-points of 3×1×2 in the first Brillouin zone were chose for calculation[17]. The self-consistent-field tolerance was set as 1.0×10^{-6} eV/atom and the Monkhorst-Pack k-point spanning grid was set as less than 0.04 $Å^{-1}$ in the Brillouin zone.

To explore the polarizability anisotropy and electronic structure of different building units, systematic calculations were implemented via the Gaussian 09 package[18] with the hybrid B3LYP functional. After that, the calculation results were analyzed by the Multiwfn 3.8 code[19].

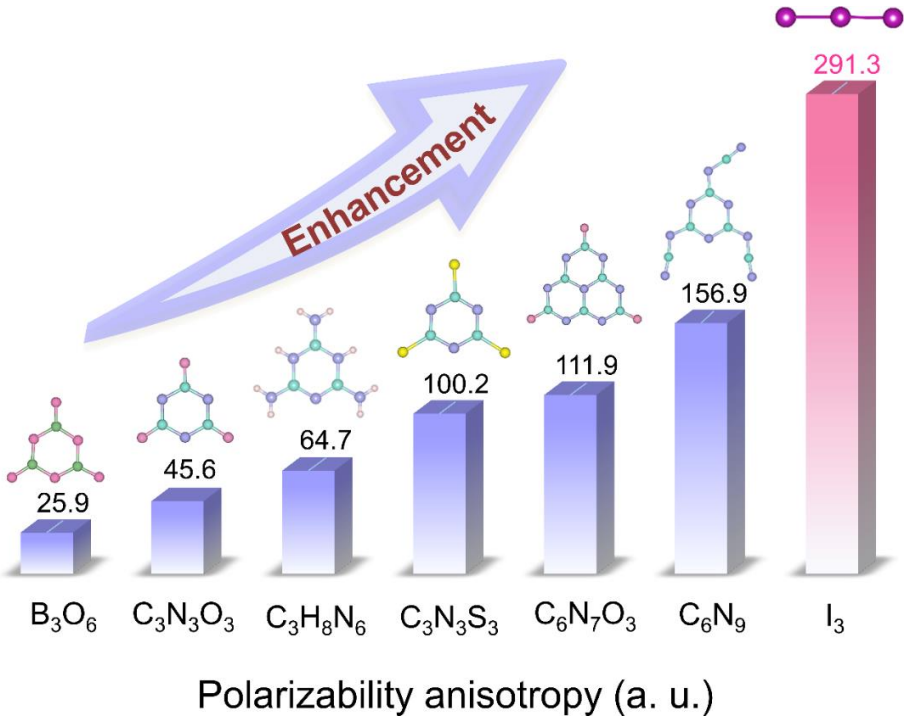

Supplementary Fig. 13 Polarizability anisotropy of $(B_3O_6)^{3-}$, $(C_3N_3O_3)^{3-}$, $(C_3H_8N_6)^{2+}$, $(C_3N_3S_3)^{3-}$, $(C_6N_7O_3)^{3-}$, $(C_6N_9)^{3-}$, and $(I_3)^-$ units.

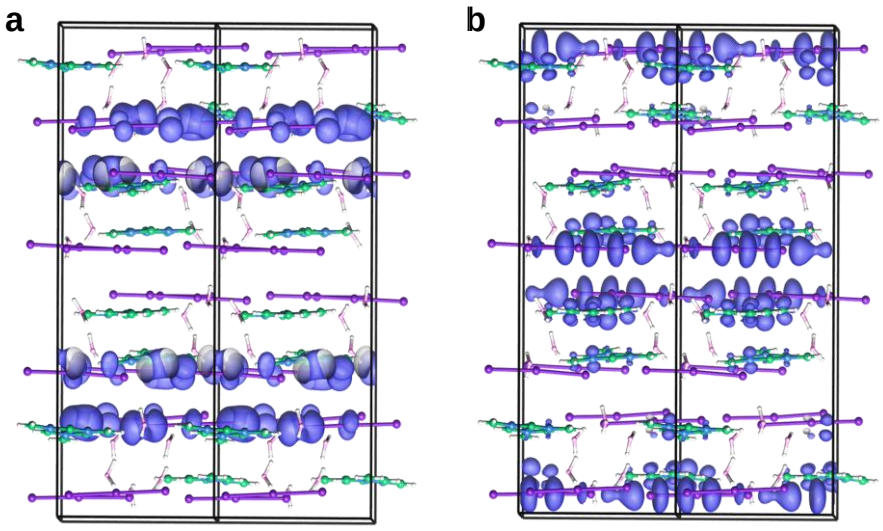

Supplementary Fig. 14 HOMO map (a) and LUMO map (b) of $C_3H_8N_6I_6 \cdot 3H_2O$. (I, C, N, O, and H atoms are represented by purple, blue-gray, navy blue, pink, and white balls, respectively.).

References

1. Segura, A. et. al. Natural optical anisotropy of h-BN: Highest giant birefringence in a bulk crystal through the mid-infrared to ultraviolet range. *Phys. Rev. Mater.* **2**, 024001 (2018).

2. Ermolaev, G. A. et al. Giant optical anisotropy in transition metal dichalcogenides for next-generation photonics. *Nat. Commun.* **12**, 854 (2014).

3. Mao, N. et al. Optical Anisotropy of Black Phosphorus in the Visible Regime. *J. Am. Chem. Soc.* **138**, 300-305 (2016).

4. Yang H, et al. Optical Waveplates Based on Birefringence of Anisotropic Two-Dimensional Layered Materials. *ACS Photonics* **4**, 3023-3030 (2017).

5. Sheldrick, G. M. A short history of SHELX. *Acta Cryst.* **64**, 112-122 (2008).

6. Dolomanov, O. V.; Bourhis, L. J.; Gildea, R. J. J. Howard, A. K. & Puschmann, H. *J. Appl. Cryst.* **42**, 339-341 (2009).

7. Spek, A. L. Single-Crystal Structure Validation with the Program PLATON. *J. Appl. Crystallogr.* **36**, 7-13 (2003).

8. Fujiwara, H. *Spectroscopic Ellipsometry: Principles and Applications*. Spectroscopic Ellipsometry: Principles and Applications. (2007).

9. Liu, S.; Chen, X. & Zhang, C. Development of a broadband Mueller matrix ellipsometer as a powerful tool for nanostructure metrology. *Thin Solid Films*. **584**, 176-185 (2015).

10. Gu, H. et. al. Layer-Dependent Dielectric and Optical Properties of Centimeter-Scale 2D WSe_2: Evolution from a Single Layer to Few Layers. *Nanoscale* **11**, 22762-22771 (2019).

11. Lautenschlager, P.; Garriga, M.; Vina, L. & Cardona, M. Temperature Dependence of the Dielectric Function and Interband Critical Points in Silicon. *Phys. Rev. B* **36**, 4821 (1987).

12. Lautenschlager, P.; Garriga, M.; Logothetidis, S. & Cardona, M. Interband Critical Points of GaAs and their Temperature Dependence. *Phys. Rev. B.* **35**, 9174-9189 (1987).

13. Kohn, W. Nobel Lecture: Electronic structure of matter-wave functions and density functionals. *Rev. Mod. Phys.* **71**, 1253-1266 (1999).

14. Clark, S. J. S., M. D.; Pickard, C. J.; Hasnip, P. J.; Probert, M. J.; Refson, K.; Payne, M. C. First principles methods using CASTEP. *Z. Kristallogr.* **220**, 567-570 (2005).

15. Perdew, J. P. Bruke, K.& Ernzerhof, M. Generalized Gradient Approximation Made Simple. *Phys. Rev. Lett*. **77**, 3865-3868 (1996).

16. Ceperley, D. M. & Alder, B. J. Ground-State of the Electron-Gas by A Stochastic Method. *Phys. Rev. Lett.* **45**, 566-569 (1980).

17. Monkhorst, H. J.; Pack, J. D. Special points for Brillouin-zone integrations. *Phys. Rev. B.* **13**, 5188-5192 (1976).

18. Frisch, M. J. Gaussian 09, Revision B.01, Gaussian, Inc., Wallingford, USA, (2009).

19. Lu, T. Chen, F. *J. Comput. Chem.* **33**, 580-592 (2012).